Research Article

Satellite Imagery Analyses of Seasonal Shifts of Vegetation Greenness at the Great Smoky Mountains National Park

Alex Larson[1], Jaemo Yang[2,*], Edylson Hernandez[1], Seung Hee Choi[1], and Jeong Chang Seong[1]

[1] School of Field Investigations & Experimental Sciences, Dr. James 'Earl' Perry College of Mathematics, Computing, and Sciences, University of West Georgia, Carrollton, GA 30118, USA; al00320@my.westga.edu; eh00128@my.westga.edu; seunghee@westga.edu; jseong@westga.edu

[2] Department of Geography, Kyung Hee University, Seoul 02447, Republic of Korea; belaw6002@khu.ac.kr

[*] Corresponding Author: belaw6002@khu.ac.kr

Academic Editor: Qi Chen
Received: 28 May 2025
Revised: 29 August 2025; 18 September 2025
Accepted: 22 September 2025
Published: 24 October 2025

Copyright: © 2025 by the authors. Submitted for open access publication under the terms and conditions of the Creative Commons Attribution (CC BY) license (https:// creativecommons.org/licenses/by/4.0/).

Abstract: This study investigates the temporal shifts in seasonal vegetation coloration, focusing on changes in greenness levels (measured by NDVI) from 1982 to 2023, using multiple satellite sources including AVHRR, Landsat, MODIS, and VIIRS. The primary objectives of this research are twofold: (1) to determine whether greenness levels have significantly changed during spring and fall, and (2) to assess whether there are notable differences in NDVI values among the various imaging sensors used. Given the context of global warming, it is plausible that greenness levels would show an increase on the same date in early spring or late fall across multiple years. Our study area consists of the Great Smoky Mountains National Park, where we analyze the timing of seasonal changes, revealing a trend toward earlier springs and longer falls. Our findings indicate significant increases in NDVI values during spring across all datasets, notably from AVHRR and Landsat, while fall data shows less consistent trends, with MODIS and VIIRS revealing minimal changes. The research highlights the importance of sensor selection in NDVI measurements, with non-parametric test results confirming significant variances among the sensors analyzed. This study contributes to understanding the implications of climate change on vegetation dynamics, underscoring the need for continued monitoring as seasonal patterns evolve.

Keywords: shift of greenness, NDVI, Great Smoky Mountains National Park, remote sensing

1. Introduction

Seasonal shifts in vegetation phenology have become increasingly noticeable: springs are arriving earlier and autumn colors emerging later. Multi-decadal analyses document significant alterations in the timing, onset, and duration of seasons, with potential long-term ecological consequences as these changes intensify (Eastman *et al*., 2013; Rozenstein & Adamowski, 2017; Calinger & Curtis, 2023; Hassan *et al*., 2023; Guo *et al*., 2024). Understanding these shifts is especially important for complex, mountainous, and largely protected forests such as the Great Smoky Mountains National Park (GSMNP), where even subtle changes in greenness can ripple through biodiversity, productivity, tourism, and ecosystem dynamics. Especially considering recent unprecedented climate anomalies, such as global warming the analysis of vegetation greenness changes over long time periods is becoming increasingly crucial.

Satellite remote sensing provides a consistent framework for quantifying vegetation greenness via the normalized difference vegetation index (NDVI), a standardized ratio of near-infrared and red reflectance that acts as a robust indicator of photosynthetic activity and ecosystem productivity (Tucker, 1979). NDVI can be computed from any multispectral sensor with visible and near-infrared bands (Huang *et al*., 2020) and is widely used across applications (e.g., Shi *et al*., 2023; Mehmood *et al*., 2024; Tuoku *et al*., 2024; Lu *et al*., 2025). NDVI is calculated by [NDVI = (NIR − Red) / (NIR + Red)], where NIR is the near-infrared band reflectance and Red is the red band reflectance; values range from −1 to +1, with healthy green vegetation typically positive. In practice, multiple sensors have been used to calculate NDVI such as Landsat (medium spatial resolution since 1972), AVHRR (1-km multispectral data across the NOAA series, 1979–2019),

Citation: Larson, A., Yang, J., Hernandez, E., Choi, S. H., & Seong, J. C. (2025). Satellite imagery analyses of seasonal shifts of vegetation greenness at the Great Smoky Mountains National Park. *Journal of Earth Observation and Geospatial Applications, 1*(1), 35–50. DOI: https://doi.org/10.65372/q71k6m39

MODIS (36 spectral bands since 1999), and VIIRS (launched in 2011 to continue and expand Earth observation as MODIS and AVHRR age). Free and open datasets obtained from those sensors, particularly, have made long-term vegetation monitoring easily accessible.

Previous research has consistently linked NDVI variability to climate drivers while documenting widespread greenness increase trends. For example, Yang *et al*. (1997) showed that NDVI changes are closely tied to temperature. Wang *et al*. (2003), using AVHRR, also found a strong relationship between temperature and NDVI at early and late growing seasons in the central Great Plains, U.S.A. At the global scale, Eastman *et al*. (2013) reported that more than half of the Earth's land surface (56.30%) exhibited significant trends, with increasing NDVI values and lengthened growing seasons in many forested areas. At the national level, Nash *et al*. (2017) found that NDVI changed significantly across 48% of the United States over 25 years, with 85% of those changes reflecting increased greenness. However, responses are not uniform: in Russia's tundra biome at the Bovanenkovo region, Lemenkova (2015) documented a decline in NDVI (1988–2011) using three Landsat TM images, attributing it to environmental and anthropogenic factors.

From a methodological perspective, extracting reliable NDVI trends from multi-sensor archives requires close attention to data quality and sensor variability. Effective use of NDVI depends on multispectral data quality and careful interpretation, given atmospheric effects, signal degradation, and sensor characteristics (Huang *et al*., 2020). Furthermore, different datasets might bring unstable consistency at different regions as different AVHRR datasets show inconstancy at Europe, Africa, and the Sahel (Beck *et al*., 2011). Concerns about sensor reliability also remain critical as demonstrated by two different camera sensors onboard unmanned aerial vehicles (Deng *et al*., 2018). Wang *et al*. (2012) also found a 0.001–0.004 yr^{-1} decline of NDVI calculated with the MODIS sensor under a simulated aerosol conditions and surface types. To address these issues, the AVHRR, MODIS, Landsat, and VIIRS datasets have been processed multiple times with new algorithms to make improved scientific time-series datasets. In the case of AVHRR, Version 6 was published in 2023 (Roger *et al*., 2023). Landsat was comprehensively reprocessed to produce Collection 2 (Crawford *et al*., 2023). MODIS datasets were reprocessed to incorporate various calibrations and corrections to produce Version 6.1 products (Vermote, 2021). VIIRS products were also reprocessed to create Version 2 (Vermote *et al*., 2023).

Along with these advances, important gaps remain in analyzing long-term vegetation responses to dynamic climate changes. One is that relatively few studies have used the recently reprocessed products that have incorporated various calibrations and corrections. It is still questionable to check if they endorse significant changes of greenness over time. The other is whether NDVI changes obtained from AVHRR, Landsat, MODIS, and VIIRS are consistent across sensors with known differences and limitations (Huang *et al*., 2020; Beck *et al*., 2011; Wang *et al*., 2012; Deng *et al*., 2018).

To fill these gaps, this study aims at analyzing vegetation greenness characteristics using the recently-reprocessed AVHRR, Landsat, MODIS, and VIIRS products spanning 1982–2023. Specifically, research objectives are (1) evaluating whether NDVI has changed significantly during spring and fall in GSMNP, and (2) assessing the extent of variation in NDVI values among sensors observing the same landscape and dates.

This study offers several key contributions. First, it provides multi-decadal trends in greenness changes with multiple sensors, focusing on a well-preserved, species-rich temperate forest landscape in the United States. Second, by analyzing the same calendar dates in both spring and fall, it directly addresses phenological transitions that are particularly relevant for climate change. Third, through a comparative analysis of newly-reprocessed AVHRR, Landsat, MODIS, and VIIRS data, while considering known data-quality and processing issues (Huang *et al*., 2020; Beck *et al*., 2011; Wang *et al*., 2012; Deng *et al*., 2018), this study highlights how sensor selection affects vegetation greenness analysis.

2. Methodology

2.1. Study Area

The Great Smoky Mountains National Park, covering approximately 2,114 km², was chosen as the study area (Figure 1) because of its rich deciduous tree population and limited human impact from 1982 to 2023. According to Walter *et al*. (2021), the Great Smoky Mountains National Park has a humid, continental climate characterized by a mean annual temperature of 13.3°C. The park receives approximately 1,400 mm of precipitation annually in the low-elevation valleys, while higher elevations receive over 2,200 mm of precipitation each year. Over 95% of the area is forested, with elevations ranging from 270 to 2,025 meters.

At elevations of 1,600 meters and above, the predominant tree species are evergreens, including hemlock (*Tsuga canadensis*), balsam fir (*Abies balsamea*), Fraser fir (*Abies fraseri*), and red spruce (*Picea rubens*). In contrast, lower elevations feature mainly deciduous trees such as tulip tree (*Liriodendron tulipifera*), red maple (*Acer rubrum*), and oak (*Quercus* spp.), alongside dense understories of evergreen shrubs like mountain laurel (*Kalmia latifolia*) and great laurel (*Rhododendron maximum*). The following shows the land cover types of the Great Smoky Mountains National Park when analyzed with the 2025 National Land Cover Dataset from the U.S. Geological Survey (2025) – Water (0.1%), Urban and Built-up (0.6%), Deciduous Forest (43.7%), Evergreen Forest (12.1%), Mixed Forest (42.8%), and Others (0.7%).

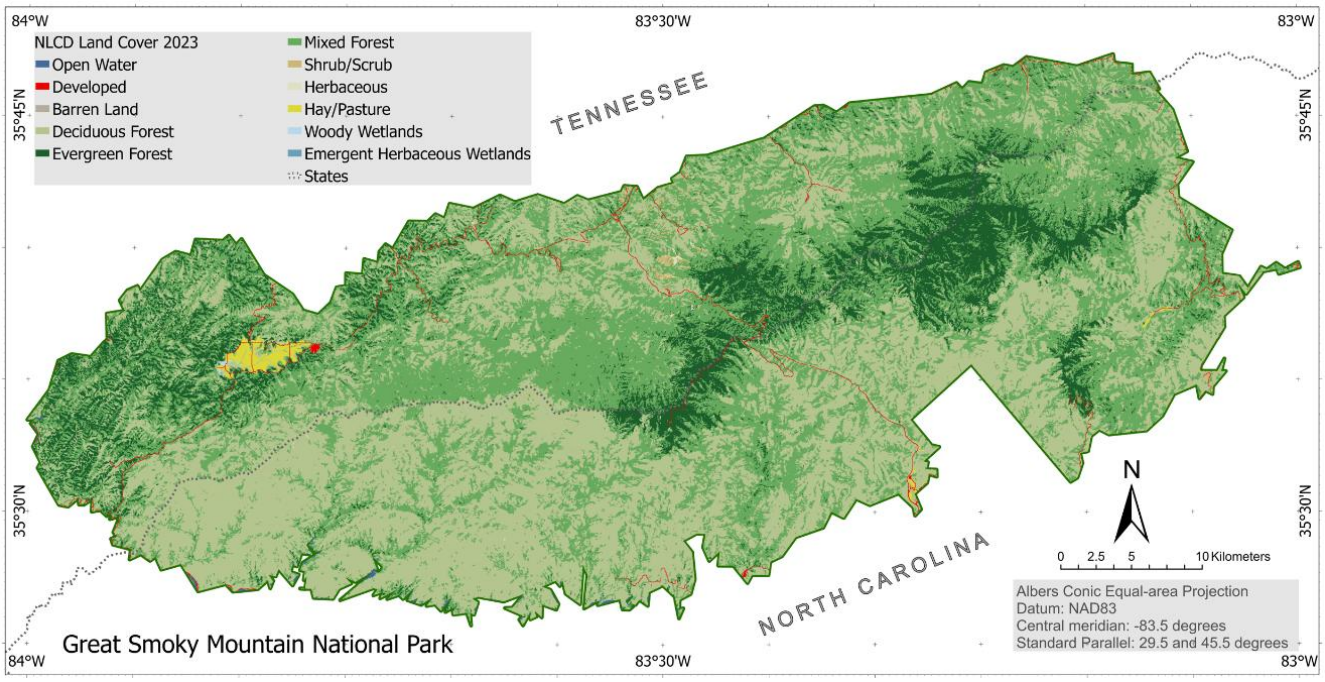

Figure 1. Study area.

2.2. Data Processing

The Google Earth Engine (GEE) and satellite imagery, courtesy of U.S. Geological Survey and NOAA, were utilized to process multi-year time-series datasets. Table 1 lists the datasets processed with GEE, while Table 2 details the specific days of each year that were selected for retrieving satellite imagery. Of the four data sources, the MODIS dataset is unique as it utilizes 8-day images to generate an 8-day composite image based on the best-quality pixels. For Landsat, images from Landsat 4, 5, 7, and 8 were used. Additionally, due to the Landsat's 16-day revisit period (or the 8-day revisit when two Landsat satellites were operational), available images were searched using the 11-day span. Cloud-contaminated pixels and Scan Line Corrector (SLC) error pixels in Landsat 7 were masked using the quality control bands included in each dataset. The average NDVI values and the count of good quality pixels were calculated with the Reducer.mean() and Reducer.count() functions, respectively. If the count of good quality pixels was fewer than 10% of total pixels, that year's dataset was excluded from the analyses. The JavaScript codes used in the GEE Code Editor are available in Appendices 2 through 5.

Table 1. Satellite imagery data sources and their product names in the Google Earth Engine.

Data Source	Dataset Name
AVHRR	NOAA CDR AVHRR: Surface Reflectance, Version 5, 1km.
Landsat	USGS Landsat (Collection 2, Surface Reflectance, Tier 1, Level 2), 30m.
MODIS	MOD09A1.061 Terra Surface Reflectance 8-Day Global 500m.
VIIRS	VNP09GA: VIIRS Surface Reflectance Daily 500m and 1km.

Table 2. The days of each year that were browsed in GEE.

Data Source	Spring Days of Each Year	Fall Days of Each Year
AVHRR	114–116	305–307
Landsat	One day between 111–121	One day between 300–310
MODIS	Composite of 114–121	Composite of 298–305
VIIRS	114–116	305–307

2.3. Statistical Analysis

For AVHRR, Landsat, or VIIRS, if multiple mean values exist for the same season, they were combined to create a grand mean. For example, the mean values of AVHRR for the 114th, 115th, and 116th days in 1982 were averaged to yield the grand mean for spring 1982. The trends in annual mean NDVI changes were then analyzed using the Mann-Kendall test (Mann, 1945; Kendall, 1975; Kenabatho, 2025) to determine if the mean values had significantly increased or decreased. Additionally, simple linear regression analysis was applied to model the trends in NDVI value changes. The use of regression analysis in this study should be viewed as exploratory, given the potential violation of statistical assumptions. Considering the long period of data collection by AVHRR and Landsat, the one-way ANOVA analysis was applied to determine if there were significant differences before and since 2001. The year 2001 was chosen because it divides the study years equally into two groups.

In order to test differences among sensors, the homoscedasticity of variances was tested first. The Brown-Forsythe test (Brown, 1974) was used because of its robustness and less sensitivity to outliers. As shown in Table 3, the Brown and Forsythe test did not detect statistically significant differences in the spring, indicating that variances can be considered equal across sensors. In contrast, it revealed significant differences in the fall, suggesting a violation of the homoscedasticity of variance assumption. The normality was also tested with the Shapiro-Wilk test on each sensor's spring and fall data. As shown in Table 4, the normality assumption is violated by the Landsat spring data and the VIIRS fall data. With the violations of homoscedasticity and normality assumptions, the Kruskal-Wallis test (Kruskal & Wallis, 1952) was performed to test differences among sensors. Furthermore, the Dunn's test (Dunn, 1964) was used to conduct pairwise comparisons.

Table 3. Brown and Forsythe test of the equality of variances.

	df_1	df_2	*F*-statistic	*p*-value
Spring	3	89	1.63	0.187
Fall	3	83	4.72	0.004

Table 4. Shapiro-Wilk normality test results (*W:* test statistic).

	AVHRR		Landsat		MODIS		VIIRS	
	Spring	Fall	Spring	Fall	Spring	Fall	Spring	Fall
Test Statistic *W*	0.960	0.971	0.806	0.985	0.959	0.954	0.959	0.822
p-value	0.283	0.625	0.000	0.972	0.427	0.325	0.753	0.017

3. Results

3.1. Trends of Annual Mean NDVI Changes

Appendix 1 presents annual mean NDVI values categorized by seasons (spring and fall) and imaging sensors (AVHRR, Landsat, MODIS, and VIIRS) from 1982 to 2023. The empty cells in the table indicate no data available due to sensor availability or image quality masks. Rows were shaded for the convenience of reading.

Figure 2 shows scatterplots of the data with linear regression and Mann-Kendall (MK) test results. The AVHRR dataset (2a and 2b) shows a positive trend in NDVI over time, particularly in the spring, where both the linear regression and Mann-Kendall tests indicate strong significance ($p < 0.05$). The fall season (2b) also shows a positive trend, though it is weaker, with a lower R^2 value and a near-significant *p*-value in the MK test. Overall, AVHRR suggests an increase in vegetation greenness over the years, especially during

springtime. The Landsat dataset (2c and 2d) presents a more mixed picture. In the spring (2c), the NDVI has a moderate upward trend, with both the regression and MK tests showing significant results. However, in the fall (2d), the trend is weak and not statistically significant. This suggests that the increase in vegetation greenness might be more prominent during the early growing season, but less so in the later months of the year.

The MODIS (2e and 2f) and VIIRS (2g and 2h) datasets show minimal changes in NDVI trends. MODIS reveals almost no significant trend in both spring and fall, with very low R^2 values and non-significant p-values, suggesting no notable changes in vegetation. VIIRS, on the other hand, shows a slight negative trend in the spring, but a significant positive trend in the fall based on the MK test, indicating potential seasonal differences in vegetation activity in more recent years. Overall, the trends across datasets suggest variability in seasonal vegetation dynamics depending on the data source.

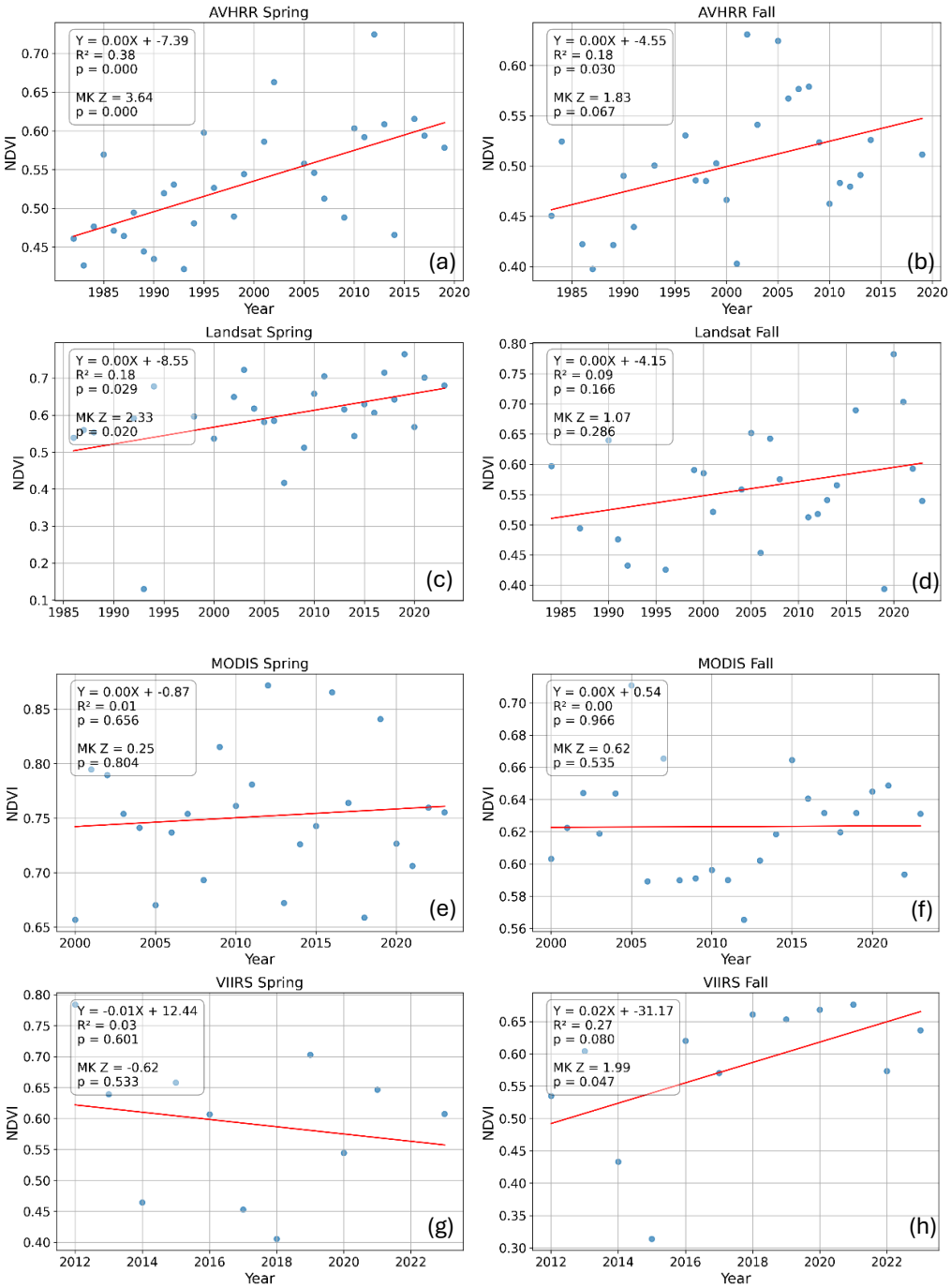

Figure 2. Scatterplots of NDVI annual changes with linear regression and Mann-Kendall tests.

3.2. Comparisons of Before and Since 2001

Table 5 compares NDVI-means before and since 2001 for the AVHRR and Landsat datasets across both spring and fall seasons. Considering the temporal coverage of dataset, AVHRR and Landsat were analyzed as they provide a much longer temporal record compared to MODIS and VIIRS.

For AVHRR Spring dataset, the NDVI mean significantly increased from 0.491 before 2001 to 0.581 since 2001. The *F*-statistic of 18.083 (df1=1, df2=29) and the very low *p*-value ($p = 0.000$) suggest that the observed increase in NDVI is statistically significant, indicating a notable change in vegetation activity in the spring season since 2001. Similarly, AVHRR Fall dataset shows a significant increase in NDVI from 0.471 to 0.529, with an *F*-statistic of 7.745 (df1=1, df2=25) and a *p*-value of 0.010, confirming that the increase in NDVI for fall is also significant, though to a lesser extent than in spring.

For the Landsat Spring dataset, there is a clear upward shift in NDVI, increasing from 0.523 before 2001 to 0.627 since 2001. The *F*-statistic of 4.835 (df1=1, df2=25) and *p*-value of 0.037 indicate that this change is statistically significant, supporting the conclusion that there has been a meaningful increase in spring vegetation as observed by Landsat since 2001. This suggests that, like AVHRR, Landsat also detects an increase in vegetation productivity in the spring season since 2001.

In contrast, the Landsat Fall data demonstrates only marginal NDVI increase from 0.530 to 0.578, which was not statistically significant as indicated by the *F*-statistic of 1.378 (df1=1, df2=22) and a *p*-value of 0.253. This suggests that vegetation activity in the fall did not experience a significant change since 2001 based on the Landsat observations, while the overall results reveal a consistent and statistically significant increase in spring NDVI. Overall, the one-way ANOVA results indicate a stronger trend of NDVI increase in spring than in fall for both datasets.

Table 5. One-way ANOVA analysis.

Dataset	NDVI Mean Before 2001	NDVI Mean Since 2001	*F*-statistic	*p*-value
AVHRR Spring	0.491	0.581	$F_{\{1,29\}} = 18.083$	0.000
AVHRR Fall	0.471	0.529	$F_{\{1,25\}} = 7.745$	0.010
Landsat Spring	0.523	0.627	$F_{\{1,25\}} = 4.835$	0.037
Landsat Fall	0.530	0.578	$F_{\{1,22\}} = 1.378$	0.253

3.3. Comparisons among Imaging Sensors

Non-parametric test methods have fewer assumptions compared to parametric test methods. They do not assume homoscedasticity of variances and normality, which makes them suitable when those assumptions are not met. In addition, non-parametric methods are based on ranks or order statistics. The Kruskal-Wallis test is one of the non-parametric methods used to compare the medians of three or more groups. It is more robust to outliers or extreme values, as it is based on rank. This test is insensitive to variability; it allows us to compare medians without assuming equal variances. The Kruskal-Wallis test result in Table 6 concludes that there are significant differences among the four sensors in both spring and fall seasons, as the *p*-values are less than the significance level 0.05.

Table 6. Kruskal-Wallis test.

		Spring Median	Fall Median
Sensor	AVHRR	0.5264	0.4911
	Landsat	0.6066	0.5621
	MODIS	0.7540	0.6210
	VIIRS	0.6073	0.6120
Kruskal-Wallis Test Results	Kruskal-Wallis *H*-statistic[1]	50.198	31.131
	df	3	3
	p-value	0.000	0.000

[1] The Kruskal-Wallis test statistic approximates a χ^2 distribution.

These results indicate that the median NDVI values measured by the sensors differ significantly, reflecting consistent variability depending on the sensor type. The magnitude of these differences, as observed in the

median ranks, suggests meaningful variations that should be carefully considered when interpreting vegetation index data across different sensors.

3.4. Pairwise Comparisons between Imaging Sensors

The Kruskal-Wallis test result indicates significant variation in the median NDVI values among the four sensors. However, it does not specify where the variation occurs. The next step is to test for pairwise differences of median for each sensor. In the case of differences, a pairwise comparison can provide information as to any statistical differences between median NDVI values for each sensor in relation to each of other sensors. The null hypothesis states that no statistically significant pairwise differences in median NDVI values were found among the four sensors. If the null hypothesis is rejected, we will have information concerning which sensor's mean NDVI values are statistically different from each of the other sensors' mean NDVI value.

The Dunn's test, a nonparametric post hoc test followed by Kruskal-Wallis test, was conducted for pairwise comparisons. It is also based on rank sums to perform multiple comparisons. Two procedures were proposed. One is to use pooled ranking across all groups (Procedure I), and the other is to use separate rankings for each comparison (Procedure II). For our case, a reference sensor is not defined, hence the Procedure I is appropriate. This examines differences across all sensor pairs. The statistic and adjusted *p*-value were computed based on the difference of Column (b) and Column (a) in Table 7, and the test statistic is approximately normal. The Holm method was applied for adjusting *p*-value during the Dunn's test. The Holm method adjusts the *p*-values in a stepwise manner. The Dunn's pairwise comparison in Table 7 shows some notable information. Among the four sensors, MODIS shows the most statistically distinct difference in both seasons. In addition, Landsat and VIIRS consistently show no significant difference, suggesting similar behavior across both seasons.

Table 7. Dunn's pairwise test.

Sensor (a)	Sensor (b)	Spring		Fall	
		Z-statistic	*p*-value[1]	*Z*-statistic	*p*-value[1]
AVHRR	Landsat	2.54	0.017*	2.48*	0.020*
	MODIS	7.02*	0.000*	5.42*	0.000*
	VIIRS	1.63	0.103	3.24*	0.003*
Landsat	AVHRR	−2.54*	0.017*	−2.48*	0.020*
	MODIS	4.42*	0.000*	2.85*	0.009*
	VIIRS	−0.27	0.395	1.22	0.223
MODIS	AVHRR	−7.02*	0.000*	−5.42*	0.000*
	Landsat	−4.42*	0.000*	−2.85*	0.009*
	VIIRS	−3.67*	0.001*	−1.11	0.133
VIIRS	AVHRR	−1.63	0.103	−3.24*	0.003*
	Landsat	0.27	0.395	−1.22	0.223
	MODIS	3.67*	0.001*	1.11	0.133

[1] Reject if $p < \alpha/2$, where $\alpha = 0.05$.

4. Discussion

The study's findings reveal notable trends in vegetation greenness, particularly an increase during spring but mixed patterns in fall. Both linear regression and Mann-Kendall tests consistently indicated similar results in NDVI changes. Specifically, the AVHRR dataset showed a significant positive trend in NDVI over time, especially in the spring ($p < 0.05$), with a weaker but still positive trend in the fall. Similarly, the Landsat dataset presented a moderate upward trend in spring, with significant results from both regression and Mann-Kendall tests. However, Landsat's fall trend was weak and not statistically significant. In contrast, the MODIS dataset showed almost no significant trend in either season, while VIIRS exhibited a slight negative trend in spring but a significant positive trend in fall based on the Mann-Kendall test. Furthermore, one-way ANOVA analyses comparing NDVI means before and since 2001 confirmed significant increases for AVHRR in both

spring (from 0.491 to 0.581, $p = 0.000$) and fall (from 0.471 to 0.529, $p = 0.010$). Landsat also showed a significant upward shift in spring (from 0.523 to 0.627, $p = 0.037$) but not in fall. Overall, these results indicate a stronger trend of NDVI increase in spring than in fall for both AVHRR and Landsat datasets.

Significant differences were observed among the imaging sensors in both spring and fall seasons, as confirmed by the Kruskal-Wallis test ($p < 0.05$). These differences suggest consistent variability in median NDVI values depending on the sensor type. Pairwise comparisons using Dunn's test revealed that MODIS demonstrated the most statistically distinct differences from other sensors in both seasons. Conversely, Landsat and VIIRS showed no significant differences from each other, indicating similar behavior across both seasons. These variations among sensors can be attributed to several factors, including differing correction methods for sensor and atmospheric effects, and the maximum-value compositing technique used, particularly in MODIS. Additionally, sensor characteristics like spatial resolution might play a role; MODIS and VIIRS provide more frequent observations but have lower spatial resolution, which may smooth out greenness trends, while Landsat's higher spatial resolution could capture more variability. The frequency of data collection also varies, with AVHRR capturing data twice per day compared to Landsat's 8 or 16-day revisit period, potentially explaining Landsat's higher standard deviation.

Despite these clear findings, the study acknowledges several limitations that could influence the interpretation of results. Firstly, missing values in some datasets might have affected the consistency of trend detection, especially in the earlier years of the study period. Secondly, the wide range of days used for MODIS (8 days) and Landsat (11 days) to create composite images might introduce instability into statistical analyses, particularly during the dynamic spring and fall transition periods. The spatial resolution of the sensors varies, with MODIS and VIIRS offering more frequent observations but lower spatial resolution, potentially leading to a smoothing of greenness trends. In contrast, Landsat's higher spatial resolution may capture more variability, suggesting that sensor characteristics inherently influence the calculated NDVI means. These suggest that users should be very careful about selecting satellite imagery products for long-term time-series studies.

Lastly, the observed shifts, particularly the notable increases in greenness during spring and mixed patterns in fall, are suggested to stem from vegetation germination processes in spring and circadian rhythms in fall that align with the diurnal cycle. The research hypothesis that annual greenness levels have risen over time, when assessed on the same dates in early spring and late fall, is largely supported for spring. The study, however, underscores the complexity of vegetation dynamics, which are influenced by various factors, including rainfall and temperature. Further ecological research on vegetation is necessary to clarify these findings in greater detail and explore the underlying biological mechanisms contributing to these seasonal shifts.

5. Conclusions

This study aimed to answer two key questions: (1) whether greenness levels have significantly changed during spring and fall since 1982, and (2) whether there are notable differences in NDVI values among the imaging sensors. The results show that NDVI values have significantly increased in spring over the study period, especially in the AVHRR and Landsat datasets. These findings underscore the potential impact of environmental changes on vegetation health, suggesting a positive response during the primary growing season. In contrast, NDVI in fall showed weaker and less consistent trends, indicating that environmental impacts might be less strong towards the end of the growing season.

Regarding sensor comparison, significant differences in NDVI values were observed across the four sensors. MODIS consistently reported higher NDVI values than AVHRR, Landsat, and VIIRS in both seasons, while AVHRR recorded the lowest. These results highlight the importance of sensor selection when analyzing or comparing NDVI data. Overall, the study confirms that both seasonal changes in vegetation and sensor characteristics play important roles in understanding long-term greenness trends.

In summary, this study demonstrates the importance of long-term vegetation monitoring using various remote sensing platforms. The significant post-2001 increase in NDVI, particularly in spring, may indicate a shift in vegetation patterns that deserves further investigation. Future research is necessary to understand the underlying factors driving these changes, including climate and plant phenology. Improved understanding of sensor performance will also support more accurate and consistent vegetation monitoring in future.

Acknowledgment: This material is based upon work partly supported by the U.S. Geological Survey under Grant/Cooperative Agreement No. G18AP00077 (for GY18-GY22) or G23AP00683 (GY23-GY27).

Conflicts of Interest: The authors declare no conflicts of interest. The funders had no role in the design of the study; in the collection, analyses, or interpretation of data; in the writing of the manuscript; or in the decision to publish the results.

References

Beck, H. E., McVicar, T. R., van Dijk, A. I., Schellekens, J., de Jeu, R. A., & Bruijnzeel, L. A. (2011). Global evaluation of four AVHRR–NDVI data sets: Intercomparison and assessment against Landsat imagery. *Remote Sensing of Environment*, 115(10), 2547–2563. https://doi.org/10.1016/j.rse.2011.05.012

Brown, M. B., & Forsythe, A. B. (1974). Robust tests for the equality of variances. *Journal of the American Statistical Association*, 69(346), 364–367. https://doi.org/10.1080/01621459.1974.10482955

Calinger K, Curtis P (2023) A century of climate warming results in growing season extension: Delayed autumn leaf phenology in north central North America. *PLoS ONE* 18(3): e0282635. https://doi.org/10.1371/journal.pone.0282635

Crawford, C. J., Roy, D. P., Arab, S., Barnes, C., Vermote, E., Hulley, G., Gerace, A., Choate, M., Engebretson, C., Micijevic, E., Schmidt, G., Anderson, C., Anderson, M., Bouchard, M., Cook, B., Dittmeier, R., Howard, D., Jenkerson, C., Kim, M., Kleyians, T., Maiersperger, T., Mueller, C., Neigh, C., Owen, L., Page, B., Pahlevan, N., Rengarajan, R., Roger, J.-C., Sayler, K., Scaramuzza, P., Skakun, S., Yan, L., Zhang, H. K., Zhu, Z., & Zahn, S. (2023). The 50-year Landsat collection 2 archive. *Science of Remote Sensing*, 8, 100103. https://doi.org/10.1016/j.srs.2023.100103

Deng, L., Mao, Z., Li, X., Hu, Z., Duan, F., & Yan, Y. (2018). UAV-based multispectral remote sensing for precision agriculture: A comparison between different cameras. *ISPRS Journal of Photogrammetry and Remote Sensing*, 146, 124–136. https://doi.org/10.1016/j.isprsjprs.2018.09.008

Dunn, O. J. (1964). Multiple comparisons using rank sums. *Technometrics*, 6(3), 241–252. https://doi.org/10.1080/00401706.1964.10490181

Eastman, J. R., Sangermano, F., Machado, E. A., Rogan, J., & Anyamba, A. (2013). Global trends in seasonality of normalized difference vegetation index (NDVI), 1982–2011. *Remote Sensing*, 5(10), 4799–4818. https://doi.org/10.3390/rs5104799

Guo, J., Wang, J., Qiao, Y., Huang, X., Smith, N. G., Liu, Z., Zhang, R., Chen, X., Wu, C., Peñuelas, J., & Chen, L. (2024). Greening-induced biophysical impacts lead to earlier spring and autumn phenology in temperate and boreal forests. *Earth's Future*. https://doi.org/10.1029/2024EF004618

Hassan, T., Gulzar, R., Hamid, M., Ahmad, R., Waza, S. A., & Khuroo, A. A. (2024). Plant phenology shifts under climate warming: A systematic review of recent scientific literature. *Environmental Monitoring and Assessment*, 196(36). https://doi.org/10.1007/s10661-023-12190-w

Huang, S., Tang, L., Hupy, J. P., Wang, Y., & Shao, G. (2020). A commentary review on the use of normalized difference vegetation index (NDVI) in the era of popular remote sensing. *Chinese Journal of Plant Ecology, 32*(8), 2711–2729. https://doi.org/10.1007/s11676-020-01155-1

Kenabatho, P. K. (2025). Innovative trend analysis of long-term spatial-temporal rainfall patterns over Botswana: Implications for water resources management. *International Journal of Remote Sensing*, 46(3), Article 102217. https://doi.org/10.1016/j.ejrh.2025.102217

Kendall, M. G. (1975). Rank correlation methods (4th ed.). Charles Griffin.

Kruskal, W. H., & Wallis, W. A. (1952). Use of ranks in one-criterion variance analysis. *Journal of the American Statistical Association*, 47(260), 583–621. https://doi.org/10.2307/2280779

Lemenkova, P. (2015). Analysis of Landsat NDVI time series for detecting degradation of vegetation. In A. N. Petin, P. V. Goleusov, & E. I. Makaseeva (Eds.), *Geoecology and sustainable use of mineral resources. From science to practice. Proceedings of 3rd International Conference of Young Scientists* (pp. 11–13). Belgorod State University. ISBN: 978-5-98242-210-1. Available at SSRN: https://ssrn.com/abstract=3312710.

Lu, Y., Yu, Y., Sun, L., Li, C., He, J., Guo, Z., Duan, L., Zhang, J., & Yu, R. (2025). NDVI-based vegetation dynamics and responses to climate change and human activities at Xinjiang from 2001 to 2020. *Scientific Reports, 15,* 25848. https://doi.org/10.1038/s41598-025-11677-5

Mann, H. B. (1945). Nonparametric tests against trend. *Econometrica*, 13(3), 245–259. https://doi.org/10.2307/1907187

Mehmood, K., Anees, S. A., Muhammad, S., Hussain, K., Shahzad, F., Liu, Q., Ansari, M. J., Alharbi, S. A., & Khan, W. R. (2024). Analyzing vegetation health dynamics across seasons and regions through NDVI and climatic variables. *Scientific Reports*, 14, Article 11775. https://doi.org/10.1038/s41598-024-62464-7

Nash, M. S., Wickham, J., Christensen, J., & Wade, T. (2017). Changes in landscape greenness and climatic factors over 25 years (1989–2013) in the USA. *Remote Sensing*, 9(3), 295. https://doi.org/10.3390/rs9030295

Roger, J. C., Santamaria Artigas, A., Ray, J. P., Villaescusa Nadal, J. L., Vermote, E. F., & Devadiga, S. (2023). *LTDR AVHRR products (Version 6) user guide* (Version 1.2). NASA Goddard Space Flight Center.

Rozenstein, O., & Adamowski, J. (2017). Linking spaceborne and ground observations of autumn foliage senescence in Southern Québec, Canada. *Remote Sensing*, 9(6), 630. https://doi.org/10.3390/rs9060630

Shi, L., Fan, H., Yang, L., Jiang, Y., Sun, Z., & Zhang, Y. (2023). NDVI-based spatial and temporal vegetation trends and their response to precipitation and temperature changes in the Mu Us Desert from 2000 to 2019. *Water Science & Technology, 88*(2), 430–442. https://doi.org/10.2166/wst.2023.212

Tucker, C. J. (1979). Red and photographic infrared linear combinations for monitoring vegetation. *Remote Sensing of Environment*, 8(2), 127–150. https://doi.org/10.1016/0034-4257(79)90013-0

Tuoku, L., Wu, Z., & Men, B. (2024). Impacts of climate factors and human activities on NDVI change in China. *Ecological Informatics, 81,* 102555. https://doi.org/10.1016/j.ecoinf.2024.102555

U.S. Geological Survey (USGS). (2025). *Annual NLCD (National Land Cover Database)—The next generation of land cover mapping: U.S. Geological Survey Fact Sheet 2025–3001* (4 p.). https://doi.org/10.3133/fs20253001. Last access:18 September 2025.

Vermote, E. (2021). MODIS/Terra surface reflectance 8-day L3 global 500m SIN grid V061. NASA Land Processes Distributed Active Archive Center. https://doi.org/10.5067/MODIS/MOD09A1.061. Last access:18 September 2025.

Vermote, E., Franch, B., & Claverie, M. (2023). VIIRS/NPP Surface Reflectance Daily L2G Global 1km and 500m SIN Grid V002. NASA Land Processes Distributed Active Archive Center. https://doi.org/10.5067/VIIRS/VNP09GA.002. Last access: 30 August 2025.

Walter, J. A., Stovall, A. E., & Atkins, J. W. (2021). Vegetation structural complexity and biodiversity in the Great Smoky Mountains. *Ecosphere*, 12(3), e03390. https://doi.org/10.1002/ecs2.3390

Wang, D., Morton, D., Masek, J., Wu, A., Nagol, J., Xiong, X., ... & Wolfe, R. (2012). Impact of sensor degradation on the MODIS NDVI time series. *Remote Sensing of Environment*, 119, 55–61. https://doi.org/10.1016/j.rse.2011.12.001

Wang, J., Rich, P. M., & Price, K. P. (2003). Temporal responses of NDVI to precipitation and temperature in the central Great Plains, USA. *International Journal of Remote Sensing*, 24(11), 2345–2364. https://doi.org/10.1080/01431160210154812

Yang, W., Yang, L., & Merchant, J. W. (1997). An assessment of AVHRR/NDVI-ecoclimatological relations in Nebraska, USA. *International Journal of Remote Sensing*, 18(10), 2161–2180. https://doi.org/10.1080/014311697217819

Appendices

Appendix 1. Annual mean NDVI values by seasons and imaging sensors.

Year	AVHRR Spring	AVHRR Fall	Landsat Spring	Landsat Fall	MODIS Spring	MODIS Fall	VIIRS Spring	VIIRS Fall
1982	0.4611							
1983	0.4265	0.4505						
1984	0.4767	0.5245		0.5971				
1985	0.5695							
1986	0.4714	0.4224	0.5391					
1987	0.4644	0.3975	0.5600	0.4939				
1988	0.4946		0.5534					
1989	0.4445	0.4214						
1990	0.4346	0.4903		0.6399				
1991	0.5195	0.4394		0.4758				
1992	0.5306		0.5917	0.4323				
1993	0.4216	0.5006	0.1303					
1994	0.4809		0.6778					
1995	0.5979							
1996	0.5264	0.5305		0.4257				
1997		0.4858						
1998	0.4897	0.4852	0.5965					
1999	0.5442	0.5027		0.5909				
2000		0.4664	0.5364	0.5853	0.6568	0.6032		
2001	0.5862	0.4028		0.5214	0.7946	0.6225		
2002	0.6631	0.6311	0.6494		0.7895	0.6440		
2003		0.5412	0.7226		0.7540	0.6188		
2004			0.6180	0.5585	0.7411	0.6438		
2005	0.5580	0.6246	0.5813	0.6519	0.6701	0.7108		
2006	0.5460	0.5674	0.5850	0.4533	0.7368	0.5892		
2007	0.5126	0.5767	0.4173	0.6426	0.7540	0.6654		
2008		0.5790		0.5756	0.6931	0.5898		
2009	0.4882	0.5236	0.5121		0.8153	0.5911		
2010	0.6033	0.4626	0.6580		0.7613	0.5963		
2011	0.5919	0.4833	0.7051	0.5124	0.7810	0.5900		
2012	0.7247	0.4796		0.5179	0.8718	0.5654	0.7841	0.5348
2013	0.6086	0.4911	0.6157	0.5409	0.6722	0.6021	0.6392	0.6042
2014	0.4657	0.5261	0.5438	0.5656	0.7261	0.6185	0.4643	0.4331
2015			0.6296		0.7427	0.6645	0.6581	0.3139
2016	0.6156		0.6066	0.6898	0.8656	0.6405	0.6067	0.6199
2017	0.5940		0.7148		0.7639	0.6316	0.4528	0.5703
2018			0.6426		0.6587	0.6196	0.4056	0.6609
2019	0.5785	0.5115	0.7646	0.3936	0.8409	0.6317	0.7031	0.6533
2020			0.5682	0.7824	0.7266	0.6450	0.5443	0.6680
2021			0.7016	0.7034	0.7061	0.6487	0.6466	0.6761
2022				0.5928	0.7597	0.5935		0.5733
2023			0.6803	0.5394	0.7553	0.6311	0.6073	0.6363

Appendix 2. Google Earth Engine Code for AVHRR

```
// Import the boundary of the Great Smoky Mountains National Park
var bnd_generalized = ee.FeatureCollection("projects/ee-geetest20/assets/bnd_generalized");

// The nTH day of year (DOY)
var nThDay = 307; // Use 114, 115, and 116 for spring; and 305, 306, and 307 for fall

// Choose the AVHRR dataset
var collection =
ee.ImageCollection('NOAA/CDR/AVHRR/NDVI/V5').filter(ee.Filter.dayOfYear(nThDay,nThDay));
var timeCollection = collection.select('TIMEOFDAY');
print(collection);

// Function to check image quality
function getQABits(image, start, end, newName) {
var pattern = 0;
  for (var i = start; i <= end; i++) {
    pattern += Math.pow(2, i); }
  return image.select([0], [newName])
  .bitwiseAnd(pattern)
  rightShift(start);
}

// Function for quality mask
function maskQuality(image) {
  var QA = image.select('QA');
  var internalQuality = getQABits(QA,0, 6, 'internal_quality_flag');
  return image.updateMask(internalQuality.eq(0));
}

// Function to choose only the images between 18:30 and 20:00 Zulu time
function timeMask(image) {
  var timeQA = image.select('TIMEOFDAY');
  return image.updateMask(timeQA.gt(1830).lt(2000));
}

// Apply masks
collection = collection.map(maskQuality).map(timeMask);

// Select only the NDVI layer
var ndviCollection = collection.select('NDVI');

// Convert annual NDVI layers to bands in an image
var ndviImage = ndviCollection.toBands();

// Apply a scale factor
ndviImage = ndviImage.multiply(0.0001);

// Calculate NDVI means
var ndviMeans = ndviImage.reduceRegion({
    reducer: ee.Reducer.mean(),
    geometry: bnd_generalized,
    scale: 1000,
    maxPixels: 1e9
  });

// Count the pixels used for calculating means
var ndviCounts = ndviImage.reduceRegion({
    reducer: ee.Reducer.count(),
    geometry: bnd_generalized,
    scale: 1000,
    maxPixels: 1e9
  });

// Print outputs
print('NDVI Means', ndviMeans);
print('NDVI Counts', ndviCounts);
```

Appendix 3. Google Earth Engine Code for Landsat

```
// 1. Define the study area
var bnd_generalized = ee.FeatureCollection("projects/eegeetest20/assets/bnd_generalized")

// 2. Setting Conditions
var start = 111; // Spring. Use 300 for fall.
var end = 121; // Spring. Use 310 for fall.
var scenePath = 19;
var sceneRow = 35;

// 3. Connect to the Landsat Surface Reflectance dataset
var L9col = ee.ImageCollection('LANDSAT/LC09/C02/T1_L2')
```

```
    .filter(ee.Filter.dayOfYear(start,end))
    .filter(ee.Filter.eq('WRS_PATH', scenePath))
    .filter(ee.Filter.eq('WRS_ROW', sceneRow))
    .map(function(image){return image.clip(bnd_generalized)});
var L8col = ee.ImageCollection('LANDSAT/LC08/C02/T1_L2')
    .filter(ee.Filter.dayOfYear(start,end))
    .filter(ee.Filter.eq('WRS_PATH', scenePath))
    .filter(ee.Filter.eq('WRS_ROW', sceneRow))
    .map(function(image){return image.clip(bnd_generalized)});
var L7col = ee.ImageCollection('LANDSAT/LE07/C02/T1_L2')
    .filter(ee.Filter.dayOfYear(start,end))
    .filter(ee.Filter.eq('WRS_PATH', scenePath))
    .filter(ee.Filter.eq('WRS_ROW', sceneRow))
    .map(function(image){return image.clip(bnd_generalized)});
var L5col = ee.ImageCollection('LANDSAT/LT05/C02/T1_L2')
    .filter(ee.Filter.dayOfYear(start,end))
    .filter(ee.Filter.eq('WRS_PATH', scenePath))
    .filter(ee.Filter.eq('WRS_ROW', sceneRow))
    .map(function(image){return image.clip(bnd_generalized)});
var L4col = ee.ImageCollection('LANDSAT/LT04/C02/T1_L2')
    .filter(ee.Filter.dayOfYear(start,end))
    .filter(ee.Filter.eq('WRS_PATH', scenePath))
    .filter(ee.Filter.eq('WRS_ROW', sceneRow))
    .map(function(image){return image.clip(bnd_generalized)});

// 4. Pre-processing
// 4.1. Apply scaling Factors
function applyScaleFactors(image) {
  var opticalBands = image.select('SR_B.').multiply(0.0000275).add(-0.2);
  var thermalBands = image.select('ST_B.*').multiply(0.00341802).add(149.0);
  return image.addBands(opticalBands, null, true)
              .addBands(thermalBands, null, true);
}

L9col = L9col.map(applyScaleFactors);
L8col = L8col.map(applyScaleFactors);
L7col = L7col.map(applyScaleFactors);
L5col = L5col.map(applyScaleFactors);
L4col = L4col.map(applyScaleFactors);

// 4.2. Select bands to be used and Rename
L9col = L9col.select('SR_B5', 'SR_B4', 'QA_PIXEL').map(function(image){return
image.rename(['NIR','RED','QA'])});
L8col = L8col.select('SR_B5', 'SR_B4', 'QA_PIXEL').map(function(image){return
image.rename(['NIR','RED','QA'])});
L7col = L7col.select('SR_B4', 'SR_B3', 'QA_PIXEL').map(function(image){return
image.rename(['NIR','RED','QA'])});
L5col = L5col.select('SR_B4', 'SR_B3', 'QA_PIXEL').map(function(image){return
image.rename(['NIR','RED','QA'])});
L4col = L4col.select('SR_B4', 'SR_B3', 'QA_PIXEL').map(function(image){return
image.rename(['NIR','RED','QA'])});

// 4.3. Merge all selected bands into a collection
var mergedCol = L4col.merge(L5col).merge(L7col).merge(L8col).merge(L9col);
print('mergedCol: ', mergedCol);
Map.addLayer(mergedCol.first().select('NIR'), {min: 0.0, max: 0.3}, 'original');

// 5. QA Bitmask processing function
function qaFunction (image) {
  var qa = image.select('QA').bitwiseAnd(parseInt('0000000000011111', 2)).eq(0);
  return image.updateMask(qa);
}
mergedCol = mergedCol.map(qaFunction);
Map.addLayer(mergedCol.first().select('NIR'), {min: 0.0, max: 0.3}, 'masked');

// 6. NDVI calculation function
var addNDVI = function(image) {
  var ndvi = image.normalizedDifference(['NIR', 'RED']).rename('NDVI');
  return image.addBands(ndvi);
};
mergedCol = mergedCol.map(addNDVI);

var mergedNDVI = mergedCol.select('NDVI');
var ndviImg = mergedNDVI.toBands();

var ndviMeans = ndviImg.reduceRegion({
    reducer: ee.Reducer.mean(),
    geometry: bnd_generalized,
    scale: 30,
    maxPixels: 1e9
});

// Print output
print('NDVI Means: ', ndviMeans);
```

Appendix 4. Google Earth Engine Code for MODIS

```
// 1. Define the study area
var bnd_generalized = ee.FeatureCollection("projects/ee-geetest20/assets/bnd_generalized");

// 2. Connect to the MODIS_500m_8day Surface Reflectance dataset and Set conditions
// 2.1. Connect to dataset and Specify the years and day of year
var collection = ee.ImageCollection('MODIS/061/MOD09A1')
    .filterBounds(bnd_generalized)
  //.filter(ee.Filter.dayOfYear(114,121)); // Landsat Spring : 114 ~ 121
    .filter(ee.Filter.dayOfYear(298,305)); // MODIS Fall : 298 ~ 305
// 2.2. Define lists to store results
var modisBands =
      ['sur_refl_b03','sur_refl_b04','sur_refl_b01','sur_refl_b02','sur_refl_b06','sur_refl_b07'];
var lsBands = ['blue','green','red','nir','swir1','swir2'];

// 3. QA Bitmask processing function
// 3.1. Helper function to extract the QA bits
function getQABits(image, start, end, newName) {
 var pattern = 0;
 for (var i = start; i <= end; i++) {
 pattern += Math.pow(2, i);
 }
 return image.select([0], [newName])
 .bitwiseAnd(pattern)
 .rightShift(start);
}

// 3.2. A function to mask out cloudy pixels.
function maskQuality(image) {
 var QA = image.select('StateQA');
 var internalQuality = getQABits(QA,8, 13, 'internal_quality_flag');
 return image.updateMask(internalQuality.eq(0));
}

// 3.3. Comparison before and after cloud masking
var noCloud = collection.map(maskQuality)
                        .select(modisBands,lsBands);
var Cloud = collection.select(modisBands,lsBands);

var visParams = {bands:['red','green','blue'],min:0,max:3000,gamma:1.3};

// 4. Apply scale factor to the image collection using the map() function
var scaleImage = function (image) {
  return image.multiply(0.0001);
};

noCloud = noCloud.map(scaleImage);

// 5. NDVI calculation function
var addNDVI = function(image) {
  var ndvi = image.normalizedDifference(['nir', 'red']).rename('NDVI');
  return image.addBands(ndvi);
};

noCloud = noCloud.map(addNDVI);

var ndviCollection = noCloud.select('NDVI');
var ndviTimeSeries = ndviCollection.toBands();

// 6. Apply Functions and Filtering
var ndviMeans = ndviTimeSeries.reduceRegion({
    reducer: ee.Reducer.mean(),
    geometry: bnd_generalized.geometry(),
    scale: 500,
    maxPixels: 1e9
});

var ndviCount = ndviTimeSeries.reduceRegion({
    reducer: ee.Reducer.count(),
    geometry: bnd_generalized.geometry(),
    scale: 500,
    maxPixels: 1e9
});

// 7. Visualizae and Print Contents
print("nvdiMeans: ", ndviMeans);
print("nvdiCount:", ndviCount);
```

Appendix 5. Google Earth Engine Code for VIIRS

```
// 1. Define the study area
var bnd_generalized = ee.FeatureCollection("projects/ee-geetest20/assets/bnd_generalized");

// 2. Connect to the VIIRS Surface Reflectance dataset
       var collection = ee.ImageCollection('NOAA/VIIRS/001/VNP09GA').filterBounds(bnd_generalized);

// 3. Setting Conditions
// 3.1. Specify the years and day of year
var startYear = 2012;
var endYear = 2023;
var nThday = 114; // Use 114, 115, and 116 for spring; 305, 306, and 307 for fall.

// 3.2. Define lists to store results
var ndviMeans = [];
var ndviCounts = [];

// 4. QF1 & QF2 Bitmask processing function
// 4.1. Helper function to extract the QA bits
function getQABits(image, start, end, newName) {
  var pattern = 0;
  for (var i = start; i <= end; i++) {
    pattern += Math.pow(2, i);
  }
  return image.select([0], [newName])
    .bitwiseAnd(pattern)
    .rightShift(start);
}

// 4.2. Function to mask out low-quality pixels based on QF1 and QF2
function maskQuality(image) {
  var qf1 = image.select('QF1');
  var qf2 = image.select('QF2');
  var cloudConfidence = getQABits(qf1, 2, 3, 'cloud_confidence');
  var cloudMask = cloudConfidence.eq(0).or(cloudConfidence.eq(1));
  var dayMask = getQABits(qf1, 4, 4, 'day_mask').eq(0);
  var sunGlintMask = getQABits(qf1, 6, 7, 'sun_glint_mask').eq(0);
  var waterMask = getQABits(qf2, 0, 2, 'water_mask').eq(1); // no desert land = 1
  var shadowMask = getQABits(qf2, 3, 3, 'shadow_mask').eq(0);
  var combinedMask = cloudMask.and(dayMask)
                              .and(sunGlintMask)
              .and(waterMask)
              .and(shadowMask)
  return image.updateMask(combinedMask);
}

// 5. NDVI calculation function
var calculateNDVI = function(image) {
  var ndvi = image.normalizedDifference(['I2', 'I1']).rename('NDVI');
  return image.addBands(ndvi);
};

// 6. Apply Functions and Filtering
      // 6.1. Function to filter collection by year and day of year, calculate NDVI, and apply mask
var filterAndCalculateNDVI = function(year, nThday) {
  return collection.filter(ee.Filter.calendarRange(year, year, 'year'))
                   .filter(ee.Filter.dayOfYear(nThday, nThday))
                   .map(calculateNDVI)
                   .map(maskQuality);
};

// 6.2. Function to calculate mean NDVI, count NDVI, and visualize the NDVI
var NDVIStatsAndVisualization = function(year, nThday) {
  var filtered = filterAndCalculateNDVI(year, nThday);
  var meanNdvi = filtered.select('NDVI').mean().reduceRegion({
    reducer: ee.Reducer.mean(),
    geometry: bnd_generalized,
    scale: 500,
    maxPixels: 1e9
  }).get('NDVI');
  var countNdvi = filtered.select('NDVI').count().reduceRegion({
    reducer: ee.Reducer.count(),
    geometry: bnd_generalized,
    scale: 500,
    maxPixels: 1e9
  }).get('NDVI');
  var clippedNdvi = filtered.select('NDVI').mean().clip(bnd_generalized);
  Map.addLayer(clippedNdvi, ndviVisParams, 'NDVI ' + year + ' DOY ' + nThday);
  return {
    'year': year,
    'dayOfYear': nThday,
    'meanNdvi': meanNdvi,
    'countNdvi': countNdvi
```

```
  };
};

// 7. Visualization
// 7.1. NDVI Visualization Function
var ndviVisParams = {
  min: 0,
  max: 1,
  palette: ['blue', 'white', 'green']
};

// 7.2. Loop through the years and collect NDVI stats and visualize
for (var year = startYear; year <= endYear; year++) {
  var stats = NDVIStatsAndVisualization(year, nThday);
  ndviMeans.push(stats.meanNdvi);
  ndviCounts.push(stats.countNdvi);
}

// 7. Print Outputs
print('NDVI Means:', ndviMeans);
print('NDVI Counts:', ndviCounts);
```

Disclaimer/Publisher's Note: The statements, opinions and data contained in all publications are solely those of the individual author(s) and contributor(s) and not of JEOGA or the editor(s). JEOGA or the editor(s) disclaim responsibility for any injury to people or property resulting from any ideas, methods, instructions or products referred to in the content. The views and conclusions contained in this document are those of the authors and should not be interpreted as representing the opinions or policies of the U.S. Geological Survey. Mention of trade names or commercial products does not constitute their endorsement by the U.S. Geological Survey.